# Low-temperature processed, stable n-i-p perovskite solar cells with indene-C60-bisadduct as electron transport material

Mohamed I. Omer[1,2] · Xizu Wang[2] · Xiaohong Tang[1]

## Abstract

Organo-metallic halide perovskites (OMHP) have proven to be promising light absorbers with superb optoelectronic properties for developing the next generation of low-cost solar cells. Over the past years, the extensive research efforts on perovskite solar cells (PSCs) have led to an impressive improvement in the photovoltaic performance on many fronts and have their main field of applications in low-temperature and low power consumption photo-electronic devices, However, a wide range of highly performing PSCs structures involves the use of metal oxide electron transport materials (ETMs) such as $TiO_2$ which requires high processing temperature that could result in a higher manufacturing energy input and cost. This also could hinder the development of low-cost and low-temperature scalable processes for device fabrication on rigid or flexible substrates. Here, we develop a low-temperature procedure (below 100 °C) that make use of Indene-C60 Bisadduct (ICBA) as an alternative ETM in the planar n-i-p-structured PSCs. After modifying the ICBA layer, we not only improved the optimum performance and stability of the device, but also study its influence on the device operation using impedance spectroscopy, and finally achieved a stabilized power conversion efficiency of 13.5%. Thereby, this study will establish low-temperature ETM as an outstanding candidate for future high stability PSCs production due to its high performance, low process temperature and easy fabrication.

## 1 Introduction

Perovskite solar cells (PSCs) have gained widespread interest over the past decade as an emerging class of photovoltaics. Ever since the early breakthroughs in the field [1, 2], organo-metallic halide perovskite (OMHP) materials has been intensely investigated for photovoltaic applications leading to an accelerated progress and ultimately achieving a record certified power conversion efficiency (PCE) of 23.7%

✉ Xizu Wang
  wangxz@imre.a-star.edu.sg

✉ Xiaohong Tang
  exhtang@ntu.edu.sg

1   Center for OptoElectronics and Biophotonics, School of Electrical & Electronic Engineering, Nanyang Technological University, Singapore 639798, Singapore

2   Institute of Materials Research and Engineering (IMRE), Agency for Science, Technology and Research, #08-03, 2 Fusionopolis Way, Innovis, Singapore 138634, Singapore

[3] in 2018, making them a prominent rival to the traditional silicon-based solar cells and already surpassing the more established thin film photovoltaic technologies based on cadmium telluride (CdTe) and copper indium gallium selenide (CIGS). This prevalent interest in OMHPs can be attributed to their attractive optoelectronic properties, such as high light absorption across the visible light spectrum [4], band-gap tunability [5], long carrier diffusion length [6, 7], small photo-exciton bending energy [8] and high defects tolerance [9] as well as the ease of processing through solution-based methods at relatively low temperatures. In order to improve the performance, reduce the fabrication cost and the processing temperature, numerous PSC structures employing a variety of organic and non-organic ETMs and HTMs have been developed for different PSC configurations. Various metal oxide n-Type materials, such as $TiO_2$, $SnO_2$ [10–12], and ZnO [13], have been studied as the ETMs for the n-i-p-structured PSCs due to their favorable conduction band alignment with that of the perovskite layer, good electron mobility, high light transmittance, and effective hole blocking. As a result with optimization, high efficiency surpassing 20% has been realized [10, 14–17]. However, metal oxide ETMs generally require a high processing temperature of

up to 500 °C with relatively long annealing time in order to obtain the highly crystallized films, and to remove the residual organic binders and residues in the case of a meso-structured layer (e.g., mesoporous $TiO_2$). This may add into the processing temperature, time, and the complexity of the PSCs production, and consequentially adding to their cost. Additionally, the required annealing temperature may limit the PSC structure to only rigid substrates that can withstand such high temperatures. Therefore, a great deal of effort went into developing low-temperature processes for PSCs to reduce the production cost and facilitate the development of flexible devices. In doing so, many strategies have focused on modifying the ETL deposition method such as using chemical bath deposition [18], pulsed-laser deposition [19], and atomic layer deposition [20, 21] to deposit the metal oxide ETL at lower temperatures. Similarly, a solution-combustion-based method was developed to replace the high temperature sol–gel process for depositing $NiO_x$ at low temperature [22]. Additionally, other metal oxides ETL like $CeO_x$ [23], $Nb_2O_5$ [24] and ZnO [25] were deposited at lower temperatures. But to this moment, $TiO_2$ remains as one of the most common ETMs in n-i-p-structured PSCs, which is used traditionally in conjunction with the excellent hole transport material (HTM) 2,2′,7,7′-tetrakis(*N*,*N*-di-*p*-methocyphenylamine)-9,9′-spirobiflurorene (Spiro-OMeTAD) for highly performing PSCs. On another note, fullerene-derived ETMs such as [6,6]-Phenyl-C61-butyric acid methyl ester ($PC_{60}BM$) and C60 are commonly used in p-i-n-structured PSCs and as interface modifier for numerous metal oxides [26–28]. Here, we investigate the fullerene derivative Indene-C60 bisadduct (ICBA) as an alternative ETM to replace $TiO_2$ in planar n-i-p configured PSCs and develop a simpler low-temperature solution process with minimal thermal annealing for the PSCs fabrication. ICBA is employed here due to its LUMO that is 0.17 eV higher than that of PCBM [29], which minimizes the energy band offset with the perovskite absorber of the PSC allowing for potentially higher Voc. Ultimately, the n-i-p-structured PSCs (FTO/ICBA/Perovskite/spiro-OMeTAD/Au) with a 13.5% stabilized PCE and an open-circuit voltage of approximately 1.1 V were fabricated at low temperature (Maximum process temperature 100 °C). Furthermore, various aspects of the device such as the perovskite morphology and crystallinity, as well as the impact of the ICBA layer thickness on the solar cell performance, were examined.

# 2 Experiment

## 2.1 PSC fabrication

Pre-patterned florine-doped tin oxide (FTO) glasses (FTO, XIN YAN TECHNOLOGY LTD) were used as the substrates. They were cleaned in an ultrasonic bath using detergent, deionized water, acetone, and isopropyl alcohol for 30, 10, 15 and 20 min, respectively. Then, they were dried with $N_2$ blowing and further cleaned using UV-ozone for 10 min at 100 °C. A thin layer of ICBA was spin-coated at various speeds (1500, 2500, and 4000 rpm) to achieve different thicknesses for the study, before being dried on a hot plate at 85 °C for 5 min. The ICBA solution was prepared by dissolving ICBA (Lumtec) in chlorobenzene with a 10 mg/mL concentration on a hot plate at 60 °C. Perovskite films were then deposited by spin-coating at 2000 rpm (200 rpm/s ramp) and 6000 rpm (2000 rpm/s ramp) for 10 and 30 s, respectively. A 400 μL of anhydrous toluene (TEDIA) was dropped on the center of the substrate 15 s before the end of the perovskite film spin-coating. The samples were then annealed on a hot plate at 100 °C for 1 h. Importantly, the perovskite precursor solution was spread out to evenly cover the entire substrate prior to spin-coating. The perovskite solution was prepared by first dissolving 1.0 M Formamidinium Iodide (Dyesol), 1.1 M PbI2 (TCI), 0.2 M PbBr2 (TCI), and 0.2 M Methylammonium Bromide (Dyesol) in a cosolvent of anhydrous *N*,*N*-dimethylformamide (sigma) and Dimethyl sulfoxide (TEDIA) with a volume ratio of 4:1, and then a 42 μL of a stock solution of 1.5 M CsI (Sigma) in DMSO was added for each milliliter of perovskite solution. Next, a thin layer of spiro-OmeTAD was deposited by spin-coating at 4000 rpm for 20 s. The Spiro-OmeTAD solution was prepared by dissolving 72 mg of Spiro-OmeTAD (Solarpur) in 1 mg of chlorobenzene, along with 29 μL of 4-tert-butylpyridine (Sigma), 17.6 μL of bis-trifluoromethanesulfonimide lithium salt (Fluka) in acetonitrile (Sigma) at a concentration of 520 mg/mL, and 29 μL of FK209 Co (III) TFSI salt (1-material) in acetonitrile (Sigma) with a concentration of 100 mg/mL. Finally, ~ 80 nm of gold was deposited on top by thermal evaporation. The fabricated devices had an active area of 0.09 $cm^2$ defined by the metal evaporation mask and FTO intersection area.

## 2.2 Characterization

I–V characteristics of the fabricated perovskite solar cells were measured under light illumination of 0.85 sun (AM 1.5G, intensity 85 $mW/cm^2$) from a solar simulator (SAN-EL ELECTRIC XEC-301S) and used KEITHLEY 2400 as a source meter. A slow voltage sweep rate of 10 mv/s was used for the measurements. No preconditioning such as light soaking or voltage bias was applied prior to the measurements of both I–V characteristics and the stabilized power conversion efficiency of the PSCs. All the I–V characteristics were measured in a nitrogen gas filled glovebox. The surface morphology of the perovskite and ICBA films was examined using scanning electron microscope (SEM) (JEOL JSM-IT100). The surface roughness

and morphology were examined using Bruker atomic force microscope (AFM) in tapping mode. The contact angle measurements of the ICBA films were taken with a contact angle video analyzer 15 s after slowly dispensing a 0.5 µL droplet of deionized water on the surface. X-ray diffraction (XRD) spectrum of the perovskite films was obtained using X-ray diffractometer (Bruker D8 DISCOVER) with a Cu Kα radiation ($\lambda = 1.54$ Å). The light absorption spectrum of the films was obtained using UV–VIS Spectrometer (Shimadzu UV-2450)), and steady-state photoluminescence (PL) measurements were performed using a HORIBA Fl-1039/40 Fluorolog with an excitation wavelength of 560 nm. Impedance spectroscopy was conducted in a nitrogen gas filled glovebox using AUTOLAB potentiostat (PGSTAT30) with an AC signal of 10 mV in amplitude, and NOVA 1.10 software package was used for the impedance spectroscopy measurements and equivalent circuit fitting.

## 3 Results and discussion

### 3.1 ICBA and perovskite films characteristics

The ICBA thin films were deposited on FTO substrates by spin-coating. To optimize the ICBA layer thickness, three spin-coating speeds were used namely 1500, 2500 and 4000 rounds per minute (r.p.m), which resulted in the layer thicknesses of 78 nm, 57 nm, and 44 nm, respectively. For simplicity, the ICBA films and PSCs fabricated using the above-mentioned thicknesses are referred to herein after as ICBA@78 nm, ICBA@57 nm and ICBA@44 nm, respectively. The texture, roughness, and hydrophobicity of the ICBA film play an important role along with other factors at modulating the perovskite film crystallization [30], grain morphology [31, 32], and ultimately affecting the solar cell performance. To assess the morphology and surface roughness of the ICBA films with different thicknesses, AFM and SEM measurements were carried out. Figure 1a–c compares the 3-dimensional AFM top surface images of the ICBA films. ICBA@78 nm film shows the lowest root-mean-square (RMS) roughness of 14.3 nm, while ICBA@57 nm and ICBA@44 nm showed a slightly higher RMS roughness values of 17.5 nm and 16.7 nm, respectively. Most importantly, the surface roughness falls within a reasonably low range that wouldn't disrupt the formation of a continuous and smooth perovskite layers deposited above. A plausible cause for the higher roughness in the case of the thinner layers could be due to the ability of thinner films to better reflect the underlying surface roughness of the substrate (i.e., FTO). Besides that, the AFM topography images reveal the granular morphology of the ICBA film, which remains as a good morphology that could facilitate an enhanced contact with perovskite layer. A similar observation can be seen from the surface SEM images shown in Figure S1.
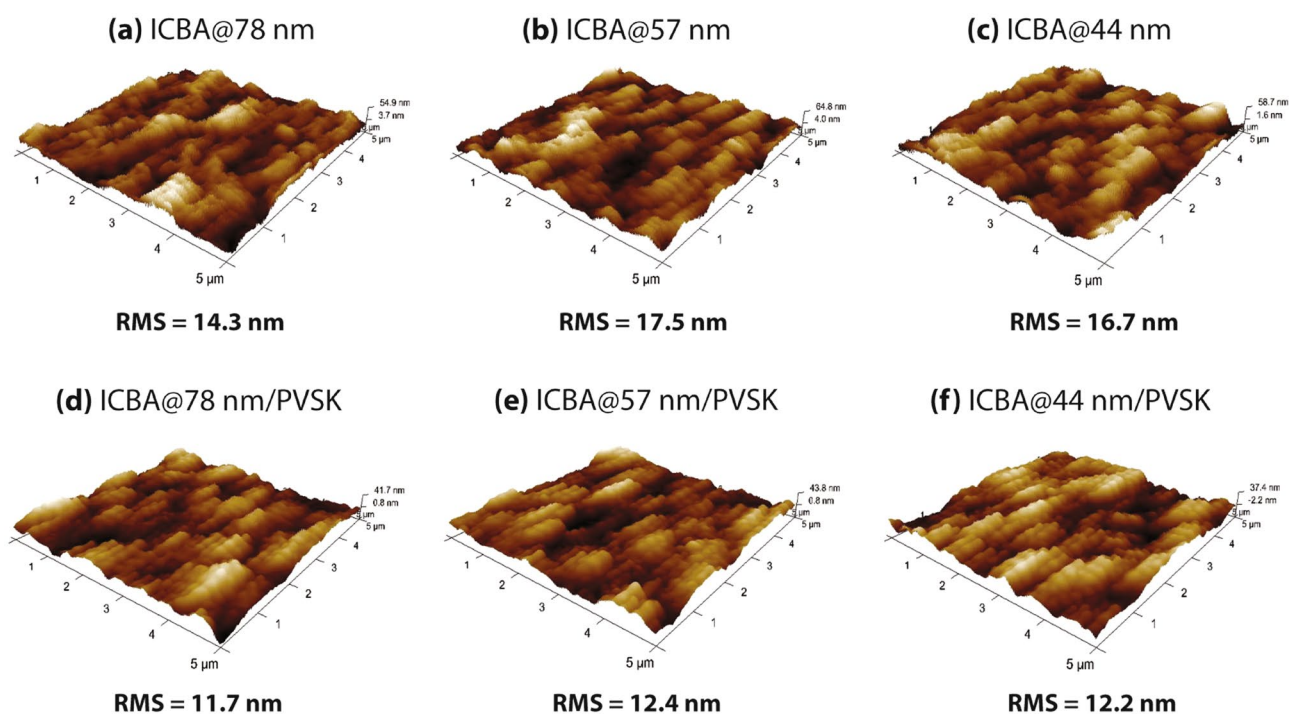


**(a)** ICBA@78 nm     **(b)** ICBA@57 nm     **(c)** ICBA@44 nm

RMS = 14.3 nm     RMS = 17.5 nm     RMS = 16.7 nm

**(d)** ICBA@78 nm/PVSK     **(e)** ICBA@57 nm/PVSK     **(f)** ICBA@44 nm/PVSK

RMS = 11.7 nm     RMS = 12.4 nm     RMS = 12.2 nm

**Fig. 1** AFM images (3D) and the corresponding RMS roughness of the bare ICBA films deposited with different thicknesses (**a–c**) and the surface topography of the perovskite films deposited on top of each ICBA layer (**d–f**), respectively

An important point to highlight regarding the ICBA films is the non-wetting nature of the films which may be of a concern when aiming to deposit perovskite films with full substrate coverage. To characterize the surface hydrophobicity, the water contact angle measurements were taken for all the ICBA films, as depicted in Figure S3. A large contact angle of around 91° was measured for both ICBA@78 nm and ICBA@57 nm while a slightly smaller contact angle of around 88° was measured for ICBA@44 nm. Overall, the ICBA surface shows a highly hydrophobic nature which requires a special attention when depositing the perovskite absorber layer on top through solution-based methods. To obtain uniform perovskite films with the full surface coverage, the hydrophobic ICBA surface was completely covered with the perovskite precursor solution prior to spin-coating. Leaving some areas uncovered would result in the films with inhomogeneous coverage. Figure S4 shows the smooth and continuous perovskite films obtained which cover the ICBA layers' surface.

The perovskite film morphology plays a critical role in the device performance and long-term stability [31]. A perovskite film with compact grain morphology and full surface coverage is favorable for the solar cell performance, as it facilitates robust charge transport and minimize carrier's recombination by reducing the recombination pathways

that could form due to direct contact between the HTM and ETM/FTO. To investigate the morphology of the perovskite films deposited on each ICBA layer through the one-step antisolvent method, SEM imaging was performed as shown in Fig. 2. All samples exhibit a similar compact grain morphology with complete surface coverage which is essential for minimizing recombination and obtaining high open-circuit voltage ($V_{oc}$) and PCE of the PSCs. However, the grain size tends to be relatively small, with an average size below 400 nm. Figure S2 shows a low magnification SEM image displaying the surface coverage over a wider area. Beside the grain morphology, the surface roughness of the perovskite absorber layer will further affect the coverage of the HTM deposited on top (i.e., Spiro-OmeTAD). Smooth perovskite films are favorable as they allow for proper surface coverage by the HTM and therefor minimize the possible direct contact between the perovskite surface and the metal electrode/external environment. To assess the surface roughness, AFM microscopy was carried out on the perovskite layers. Figure 1d–f shows the 3-dimensional AFM images and the corresponding RMS roughness of each sample. Importantly, all films show a reasonably low roughness which falls in the range between 11.7 and 12.2 nm.

Beside morphology, the crystallinity and phase purity of the perovskite film play an important role in it's
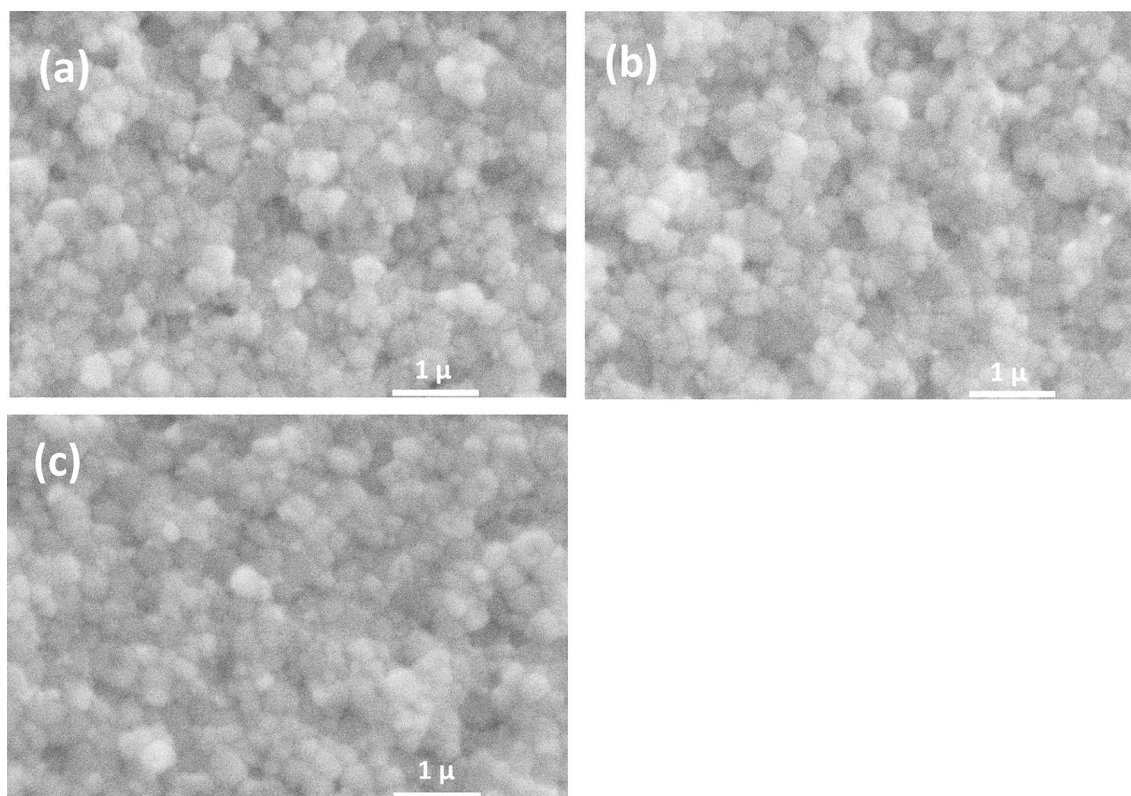


**Fig. 2** Top view SEM images of the perovskite films spin-coated on top of **a** ICBA@78 nm, **b** ICBA@57 nm and **c** ICBA@44 nm films, respectively
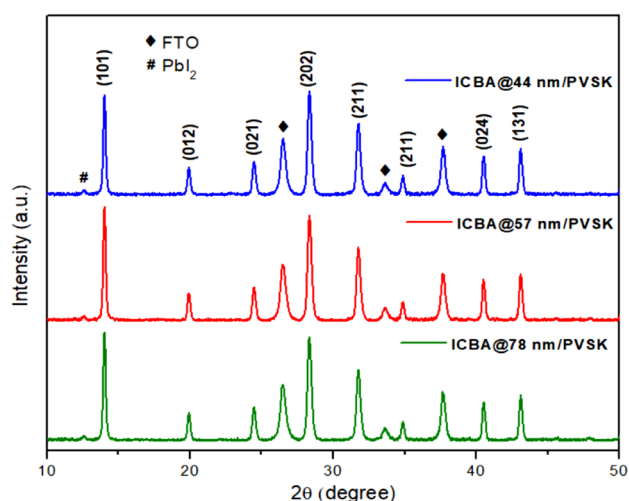
**Fig. 3** X-ray diffraction pattern of the perovskite films deposited on top of 44, 57, and 78 nm thick ICBA layers

optoelectronic properties and consequently the device performance. To investigate the crystallinity of the perovskite films deposited on the ICBA layers, XRD spectrum of the perovskite films was measured as shown in Fig. 3. All samples reveal a clear diffraction peak at ~ 14° which is characteristic of the perovskite (101) plane. While the weak peak at 12.7° corresponds to a negligible amount of unreacted cubic $PbI_2$, this indicates a complete conversion of the precursor into the perovskite photoactive phase. With regard to crystallinity, all samples show a high degree of crystallinity with a narrow full width half maximum (FWHM, based on the 14° peak) of 0.211, 0.212, and 0.206 for the films deposited on 78, 57, 44 nm ICBA, respectively. Overall, these results indicate that phase pure high-quality crystallized perovskite films [33] are obtainable on top of the hydrophobic ICBA layer.

## 3.2 Optical absorption and photoluminescence

ICBA has higher light absorption in the visible spectrum range than that of PCBM and Indene-C60 monoadduct (ICMA), which made it an attractive option earlier in OPV researches [29]. However, for our purpose, ICBA may introduce significant parasitic absorption if it's too pronounced and therefor limits the PSC performance. To evaluate the absorption of the ICBA films in comparison with that of the perovskite, the UV–visible light absorption spectrum of the films was measured as shown in Figure S5. The ICBA films reveal a limited absorption spectrum which picks up in the wavelengths below 550 nm, with no absorption in the remnant visible light range. Furthermore, in comparison with the perovskite absorption, it can be noted that the parasitic ICBA's absorption in the range below 550 nm is minuscule.

Therefore, it is reasonable to suggest that the parasitic absorption here is insignificant and has minimum potential for negatively impacting the overall PSC performance.

Steady-state photoluminescence (PL) is a commonly employed technique to examine the carriers' extraction at the perovskite/ETM or HTM interfaces and assess the quenching efficacy of various carriers' transport materials. Here, we carried out the steady state PL measurements to assess and compare the electron extraction and transfer at the interface between the perovskite absorber and the different thickness ICBA layers. A perovskite film deposited on glass was used as a reference sample. As seen from Fig. 4, all ICBA films result in PL quenching in comparison with the reference sample, which is indicative of effective electron extraction by the ICBA films. The thinnest ICBA film (i.e., 44 nm), however, shows a relatively lower PL quenching in comparison with the thicker ones, indicating a retarded electron transfer, which is possibly due to an incomplete substrate coverage by the ICBA layer or/and an improper interface formation which minimizes its effective contact with the perovskite absorber. The ICBA@57 nm film results in the best PL quenching which indicates an enhanced charge transfer. The normalized-PL spectrum shown in Figure S6 reveals no clear wavelength shift or significant peak broadening.

## 3.3 Photovoltaic performance

To examine the devices' performance, 24 PSCs with different ICBA thickness were fabricated (in three groups) using the antisolvent method. Table 1 summarizes each ICBA thickness PSC and figures of merit (FOM) obtained for each device group based on a reverse sweep I–V characteristic.
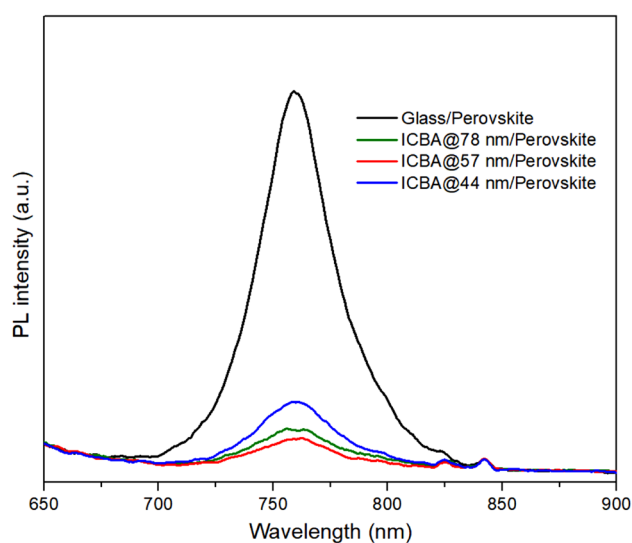


**Fig. 4** Steady-state photoluminescence of perovskite films deposited on glass and ICBA layers

**Table 1** Summary of the figures of merit and ICBA thickness of each group device group

| | | $V_{oc}$ (V) | $J_{sc}$ (mA/cm²) | FF (%) | PCE (%) | ICBA thickness |
|---|---|---|---|---|---|---|
| ICBA@78 nm | Best cell | 1.096 | 18.66 | 59.71 | 14.18 | |
| | Average | 1.0326 ± 0.08 | 18.71 ± 0.26 | 56.73 ± 2.42 | 12.9 ± 1.41 | ~78 nm |
| ICBA@57 nm | Best cell | 1.092 | 19.22 | 60.29 | 14.71 | |
| | Average | 1.070 ± 0.013 | 18.71 ± 0.31 | 59.77 ± 0.68 | 14.06 ± 0.43 | ~57 nm |
| ICBA@44 nm | Best cell | 1.040 | 18.16 | 52.08 | 11.58 | |
| | Average | 1.015 ± 0.059 | 18.07 ± 0.27 | 50.88 ± 2.25 | 10.98 ± 0.92 | ~44 nm |

Overall, the ICBA@78 nm and ICBA@57 nm PSC groups show a similar average short circuit current ($J_{sh}$) and fill factor (FF). However, the ICBA@57 group exhibits a higher average open-circuit voltage ($V_{oc}$) of 1.07 V which resulted in a higher average PCE of 14.0% compared to 12.9% for the ICBA@78 nm group. On the other hand, the ICBA@44 nm PSCs show the lowest average PCE of 10.98% primarily due to the reduced FF and $V_{oc}$. It's notable here that all groups show a similar short circuit current of around 18 mA/cm and the variation in performance mainly lies in the $V_{oc}$ and FF. It's worth noting that a slow scan rate of 10 mv/s was used for the I–V characteristics measurements as it reflects a more accurate representation of the FOMs, compared with faster scan rates that could result in over/under estimation of some FOMs.

Figure 5a shows the I–V curves of the champion device of each group of the PSCs. The I–V characteristics display a hysteresis behavior, which is commonly observed in a wide array of PSCs, particularly with n-i-p-structured devices. Various mechanisms such as ion migration and interfacial charge trapping/de-trapping were proposed as the driving factors [34–36]. To obtain a more accurate picture of the PCE of the devices, the stabilized power conversion efficiency (s-PCE) at the maximum power point for the champion device from each group was measured with no preconditioning, as shown in Fig. 5b. The highest s-PCE of 13.5% was measured for the ICBA@57 nm device, a similar efficiency of 13.34% was recorded for the ICBA@78 nm PSC, while the ICBA@44 nm device showed the lowest s-PCE of 9.92%. Despite ICBA@57 nm showing the best performance with the fastest stabilization time, ICBA@78 nm gave a slightly lower but yet comparable performance for both the FOMs and the s-PCE (both are between 13 and 14%). In contrast, the ICBA@44 nm showed a much lower performance for both FOMs and s-PCE measurements (< 10%) which is due to the lower FF and $V_{oc}$. The fast stabilization time and higher power output exhibited by the ICBA@57 nm device indicate that a ~ 57 nm ICBA thickness and it's corresponding layer morphology results in an optimum carrier extraction that is less impeded by the slow
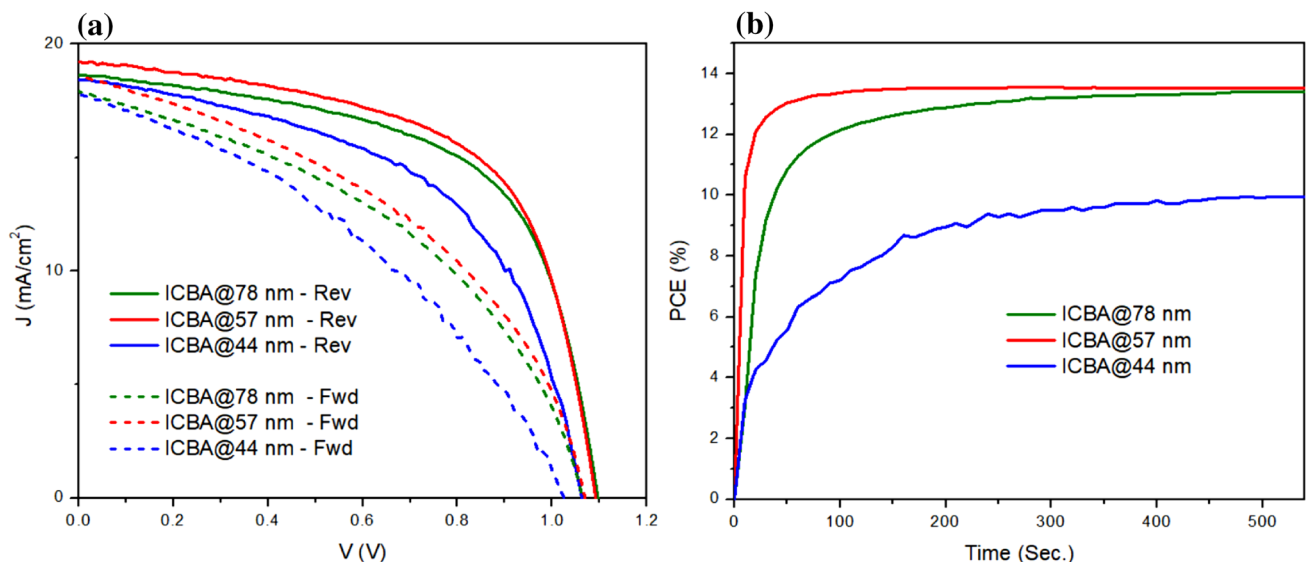


**Fig. 5** **a** I–V characteristics of the PSCs measured by forward (solid line) and reverse (dashed lines) voltage sweeps. **b** Stabilized power conversion efficiency of the champion devices of each group

dynamic response of the device, in addition to lower recombination losses as will be revealed in the following section by impedance spectroscopy. Furthermore, the stable power output at maximum power point for more than 8 min by the three different thicknesses indicates that an ICBA layer can function as a stable ETM in n-i-p perovskite devices.

## 3.4 Electrical impedance spectroscopy

Electrical impedance spectroscopy (EIS) was utilized to study the carrier's recombination in the devices. Figure 6a shows the Nyquist plots obtained from the measurements conducted under dark conditions with an applied forward bias of 800 mV. The inset figure depicts the equivalent circuit used for fitting the spectrum [37], which is constituted of an ohmic series resistance of the conducting substrate and external contacts $R_s$, the geometric capacitance $C_1$, the contacts charge transport resistance $R_1$, the chemical capacitance contribution $C_2$, and the Recombination resistance $R_{rec}$. Table S1 summarizes the recombination resistance values obtained for each device. Both ICBA@78 nm and ICBA@44 nm devices exhibit a recombination resistance values of 1.33 kΩ and 1.04 kΩ, respectively, which is lower than the 2.3 kΩ value obtained for ICBA@57 nm PSC. This indicates a lower carrier's recombination rate for ICBA@57 nm devices, which may help explain the higher conversion efficiency and $V_{oc}$ obtained with this group of devices.

On another front, the dark current characteristics in Fig. 6b reveal a similar trend. The inset figure shows the I–V characteristics around 0 V. It's evident that ICBA@44 nm PSC has the highest leakage current in the reverse bias while ICBA@57 nm PSC shows the lowest leakage current. Additionally, the dark current onset in the forward bias occurs at a much lower voltage for ICBA@44 nm PSC and a much higher voltage of around 0.8 V for ICBA@57 nm PSC, which is in consistency with the recombination resistance trend obtained from EIS data.

With photovoltaic device, shunt current losses can result from shunting pathways that are caused by the structural defects, impurities, and inhomogeneity arising during the fabrication process. These losses, especially if they are pronounced, would limit the solar cell $V_{oc}$ and power output under illumination. Given that the morphology and crystallinity of the perovskite layer shows no significant difference between the device groups, a plausible cause for the lower recombination resistance in the case of the thinnest ICBA layers could be due to structural recombination pathways that are formed between the perovskite absorber and FTO.

In conclusion, an ICBA layer with a thickness of around 57 nm (obtained by spin-coating 10 mg/mL solution at 2500 r.p.m) resulted in an optimum performance with the highest recombination resistance, a thicker layer of 78 nm resulted in a lower but yet comparable performance. While the thinnest layer with a thickness of 44 nm resulted in the poorest performance and lowest $V_{oc}$ which was attributed to higher recombination rates driven by shunt losses, in addition to the lower carrier extraction rate indicated by lower PL quenching.
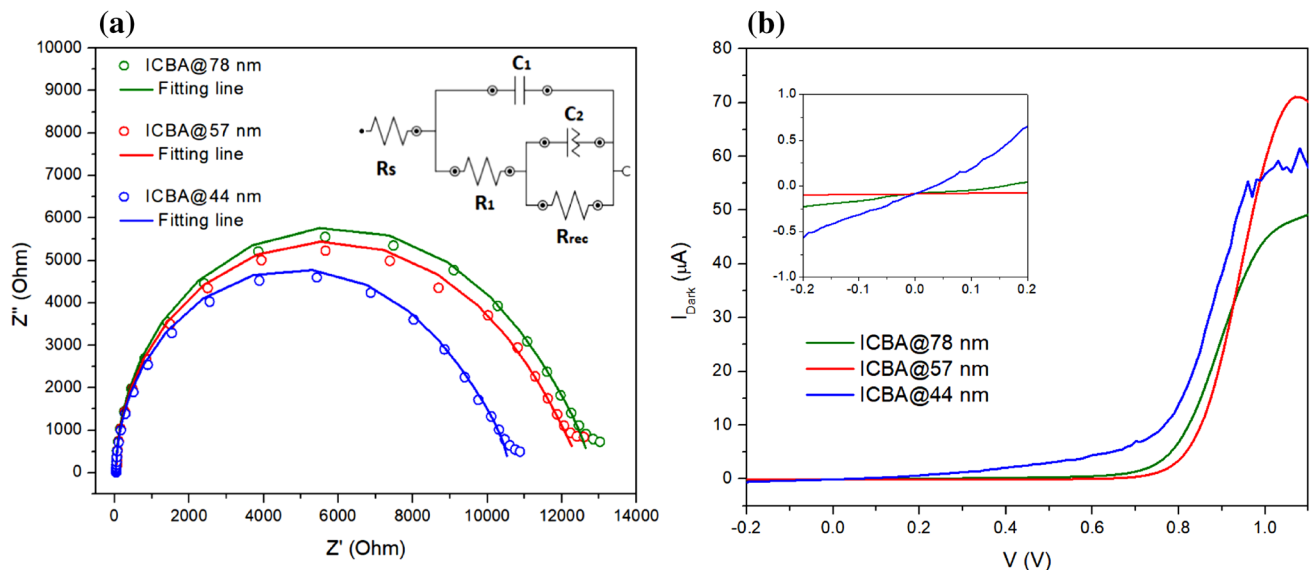


**Fig. 6** **a** Nyquist plot with the equivalent circuit used for fitting in the inset figure. **b** dark I–V characteristics for perovskite with different ICBA thickness. Inset graph in **b** shows a close-up view of the I–V curve around 0 V

# 4 Conclusion

In conclusion, planar PSCs with a structure of (FTO/ICBA/Perovskite/Spiro-OmeTAD/Au) were fabricated at low temperature of 100 °C and a stabilized PCE of 13.5% was achieved. ICBA was used effectively as an ETM layer to replace the traditional metal oxide ETM (i.e., $TiO_2$) deposited below the perovskite layer in an n-i-p-structured PSC device and realize a simpler fabrication procedure. An optimized ICBA layer results in a good electron collection and effective hole blocking, besides being stable and easily deposited through spin-coating. Despite being highly hydrophobic, smooth and phase pure perovskite films with high crystallinity and compact grain morphology were deposited on top of ICBA films through a single-step solution process (i.e., antisolvent method). Furthermore, the influence of the ICBA layer thickness on the device performance was examined through impedance spectroscopy and dark I–V characteristics. A thickness of around 57 nm of the ICBA layer resulted in an optimum performance PSC which was attributed to reduced recombination in the device while a thinner layer was found to be detrimental to performance as it encourages shunt losses and recombination, resulting in lower $V_{oc}$ and FF. Additionally, ICBA films were revealed to be sufficiently transparent and poorly absorptive within a limited wavelength region below 550 nm which makes it a suitable option to utilize for efficient flexible PSCs. Based on impedance spectroscopy analysis, the different ETM deposition conditions and thickness results in different recombination rates in the devices. As a result, further optimization and improvement of the ICBA film preparation methodology could potentially improve its electronic characteristics (e.g., energetic disorder) to enhance its performance in perovskite devices.

## Compliance with ethical standards

# References

1. A. Kojima, K. Teshima, Y. Shirai, T. Miyasaka, Organometal halide perovskites as visible-light sensitizers for photovoltaic cells. J. Am. Chem. Soc. **131**, 6050–6051 (2009). https://doi.org/10.1021/ja809598r

2. H.-S. Kim, C.-R. Lee, J.-H. Im, K.-B. Lee, T. Moehl, A. Marchioro, S.-J. Moon, R. Humphry-Baker, J.-H. Yum, J.E. Moser, M. Grätzel, N.-G. Park, Lead iodide perovskite sensitized all-solid-state submicron thin film mesoscopic solar cell with efficiency exceeding 9%. Sci. Rep. **2**, 591 (2012). https://doi.org/10.1038/srep00591

3. Best Research-Cell Efficiencies (NREL). https://www.nrel.gov/pv/assets/pdfs/pv-efficiency-chart.20181221.pdf. Accessed 25 Feb 2019

4. J.H. Noh, S.H. Im, J.H. Heo, T.N. Mandal, S.I. Seok, Chemical management for colorful, efficient, and stable inorganic–organic hybrid nanostructured solar cells. Nano Lett. **13**, 1764–1769 (2013). https://doi.org/10.1021/nl400349b

5. N.-G. Park, Perovskite solar cells: an emerging photovoltaic technology. Mater. Today **18**, 65–72 (2015). https://doi.org/10.1016/j.mattod.2014.07.007

6. S.D. Stranks, G.E. Eperon, G. Grancini, C. Menelaou, M.J.P. Alcocer, T. Leijtens, L.M. Herz, A. Petrozza, H.J. Snaith, Electron-hole diffusion lengths exceeding 1 micrometer in an organometal trihalide perovskite absorber. Science **342**, 341–344 (2013). https://doi.org/10.1126/science.1243982

7. G. Xing, N. Mathews, S. Sun, S.S. Lim, Y.M. Lam, M. Gratzel, S. Mhaisalkar, T.C. Sum, Long-range balanced electron- and hole-transport lengths in organic-inorganic CH3NH3PbI3. Science **342**, 344–347 (2013). https://doi.org/10.1126/science.1243167

8. Y. Yamada, T. Nakamura, M. Endo, A. Wakamiya, Y. Kanemitsu, Photocarrier recombination dynamics in perovskite CH 3 NH 3 PbI 3 for solar cell applications. J. Am. Chem. Soc. **136**, 11610–11613 (2014). https://doi.org/10.1021/ja506624n

9. W.-J. Yin, T. Shi, Y. Yan, Unusual defect physics in CH3NH3PbI3 perovskite solarcell absorber. Appl. Phys. Lett. **104**, 063903 (2014)

10. E.H. Anaraki, A. Kermanpur, L. Steier, K. Domanski, T. Matsui, W. Tress, M. Saliba, A. Abate, M. Grätzel, A. Hagfeldt, J.-P. Correa-Baena, Highly efficient and stable planar perovskite solar cells by solution-processed tin oxide. Energy Environ. Sci. **9**, 3128–3134 (2016). https://doi.org/10.1039/C6EE02390H

11. Q. Wali, Y. Iqbal, B. Pal, A. Lowe, R. Jose, Tin oxide as an emerging electron transport medium in perovskite solar cells. Sol. Energy Mater. Sol. Cells **179**, 102–117 (2018). https://doi.org/10.1016/j.solmat.2018.02.007

12. W. Ke, G. Fang, Q. Liu, L. Xiong, P. Qin, H. Tao, J. Wang, H. Lei, B. Li, J. Wan, G. Yang, Y. Yan, Low-temperature solution-processed tin oxide as an alternative electron transporting layer for efficient perovskite solar cells. J. Am. Chem. Soc. **137**, 6730–6733 (2015). https://doi.org/10.1021/jacs.5b01994

13. P. Zhang, J. Wu, T. Zhang, Y. Wang, D. Liu, H. Chen, L. Ji, C. Liu, W. Ahmad, Z.D. Chen, S. Li, Perovskite solar cells with ZnO electron-transporting materials. Adv. Mater. **30**, 1703737 (2018). https://doi.org/10.1002/adma.201703737

14. M. Saliba, T. Matsui, J.-Y. Seo, K. Domanski, J.-P. Correa-Baena, M.K. Nazeeruddin, S.M. Zakeeruddin, W. Tress, A. Abate, A. Hagfeldt, M. Grätzel, Cesium-containing triple cation perovskite solar cells: improved stability, reproducibility and high efficiency. Energy Environ. Sci. **9**, 1989–1997 (2016). https://doi.org/10.1039/C5EE03874J

15. H. Tan, A. Jain, O. Voznyy, X. Lan, F.P. García de Arquer, J.Z. Fan, R. Quintero-Bermudez, M. Yuan, B. Zhang, Y. Zhao, F. Fan, P. Li, L.N. Quan, Y. Zhao, Z.-H. Lu, Z. Yang, S. Hoogland, E.H. Sargent, Efficient and stable solution-processed planar perovskite solar cells via contact passivation. Science **355**, 722–726 (2017). https://doi.org/10.1126/science.aai9081

16. T. Ye, M. Petrović, S. Peng, J.L.K. Yoong, C. Vijila, S. Ramakrishna, Enhanced charge carrier transport and device performance through dual-cesium doping in mixed-cation perovskite solar cells with near unity free carrier ratios. ACS Appl. Mater.

Interfaces **9**, 2358–2368 (2017). https://doi.org/10.1021/acsami.6b12845

17. A. Klasen, P. Baumli, Q. Sheng, E. Johannes, S.A. Bretschneider, I.M. Hermes, V.W. Bergmann, C. Gort, A. Axt, S.A.L. Weber, H. Kim, H.-J. Butt, W. Tremel, R. Berger, Removal of surface oxygen vacancies increases conductance through TiO 2 thin films for perovskite solar cells. J. Phys. Chem. C **123**, 13458–13466 (2019). https://doi.org/10.1021/acs.jpcc.9b02371

18. X. Chen, L.J. Tang, S. Yang, Y. Hou, H.G. Yang, A low-temperature processed flower-like TiO 2 array as an electron transport layer for high-performance perovskite solar cells. J. Mater. Chem. A **4**, 6521–6526 (2016). https://doi.org/10.1039/C6TA00893C

19. B. Yang, M. Mahjouri-Samani, C.M. Rouleau, D.B. Geohegan, K. Xiao, Low temperature synthesis of hierarchical TiO 2 nanostructures for high performance perovskite solar cells by pulsed laser deposition. Phys. Chem. Chem. Phys. **18**, 27067–27072 (2016). https://doi.org/10.1039/C6CP02896A

20. Y. Kuang, V. Zardetto, R. van Gils, S. Karwal, D. Koushik, M.A. Verheijen, L.E. Black, C. Weijtens, S. Veenstra, R. Andriessen, W.M.M. Kessels, M. Creatore, Low-temperature plasma-assisted atomic-layer-deposited SnO$_2$ as an electron transport layer in planar perovskite solar cells. ACS Appl. Mater. Interfaces **10**, 30367–30378 (2018). https://doi.org/10.1021/acsami.8b09515

21. D. Chen, A. Su, X. Li, S. Pang, W. Zhu, H. Xi, J. Chang, J. Zhang, C. Zhang, Y. Hao, Efficient planar perovskite solar cells with low-temperature atomic layer deposited TiO$_2$ electron transport layer and interfacial modifier. Sol. Energy **188**, 239–246 (2019). https://doi.org/10.1016/j.solener.2019.06.016

22. Z. Liu, J. Chang, Z. Lin, L. Zhou, Z. Yang, D. Chen, C. Zhang, S.F. Liu, Y. Hao, High-performance planar perovskite solar cells using low temperature, solution-combustion-based nickel oxide hole transporting layer with efficiency exceeding 20%. Adv. Energy Mater. **8**, 1703432 (2018). https://doi.org/10.1002/aenm.201703432

23. X. Wang, L.-L. Deng, L.-Y. Wang, S.-M. Dai, Z. Xing, X.-X. Zhan, X.-Z. Lu, S.-Y. Xie, R.-B. Huang, L.-S. Zheng, Cerium oxide standing out as an electron transport layer for efficient and stable perovskite solar cells processed at low temperature. J. Mater. Chem. A **5**, 1706–1712 (2017). https://doi.org/10.1039/C6TA07541J

24. X. Ling, J. Yuan, D. Liu, Y. Wang, Y. Zhang, S. Chen, H. Wu, F. Jin, F. Wu, G. Shi, X. Tang, J. Zheng, S. Liu, Z. Liu, W. Ma, Room-temperature processed Nb$_2$O$_5$ as the electron-transporting layer for efficient planar perovskite solar cells. ACS Appl. Mater. Interfaces **9**, 23181–23188 (2017). https://doi.org/10.1021/acsami.7b05113

25. J. Ma, Z. Lin, X. Guo, L. Zhou, J. Su, C. Zhang, Z. Yang, J. Chang, S. Liu, Y. Hao, Low-temperature solution-processed ZnO electron transport layer for highly efficient and stable planar perovskite solar cells with efficiency over 20%. Sol. RRL **3**, 1900096 (2019). https://doi.org/10.1002/solr.201900096

26. H. Jiang, G. Jiang, W. Xing, W. Xiong, X. Zhang, B. Wang, H. Zhang, Y. Zheng, High current density and low hysteresis effect of planar perovskite solar cells via PCBM-doping and interfacial improvement. ACS Appl. Mater. Interfaces **10**, 29954–29964 (2018). https://doi.org/10.1021/acsami.8b06020

27. X. Guo, B. Zhang, Z. Lin, J. Ma, J. Su, W. Zhu, C. Zhang, J. Zhang, J. Chang, Y. Hao, Interface engineering of TiO2/perovskite interface via fullerene derivatives for high performance planar perovskite solar cells. Org. Electron. **62**, 459–467 (2018). https://doi.org/10.1016/j.orgel.2018.08.039

28. J. Kim, G. Kim, T.K. Kim, S. Kwon, H. Back, J. Lee, S.H. Lee, H. Kang, K. Lee, Efficient planar-heterojunction perovskite solar cells achieved via interfacial modification of a sol–gel ZnO electron collection layer. J. Mater. Chem. A **2**, 17291–17296 (2014). https://doi.org/10.1039/C4TA03954H

29. Y. He, H.-Y. Chen, J. Hou, Y. Li, Indene−C 60 bisadduct: a new acceptor for high-performance polymer solar cells. J. Am. Chem. Soc. **132**, 1377–1382 (2010). https://doi.org/10.1021/ja908602j

30. H. Li, Y. Xue, B. Zheng, J. Tian, H. Wang, C. Gao, X. Liu, Interface modification with PCBM intermediate layers for planar formamidinium perovskite solar cells. RSC Adv. **7**, 30422–30427 (2017). https://doi.org/10.1039/C7RA04311B

31. C. Bi, Q. Wang, Y. Shao, Y. Yuan, Z. Xiao, J. Huang, Non-wetting surface-driven high-aspect-ratio crystalline grain growth for efficient hybrid perovskite solar cells. Nat. Commun. **6**, 7747 (2015). https://doi.org/10.1038/ncomms8747

32. L. Zheng, D. Zhang, Y. Ma, Z. Lu, Z. Chen, S. Wang, L. Xiao, Q. Gong, Morphology control of the perovskite films for efficient solar cells. Dalton Trans. **44**, 10582–10593 (2015). https://doi.org/10.1039/C4DT03869J

33. T. Ye, S.-L. Lim, X. Li, M. Petrović, X. Wang, C. Jiang, W.-P. Goh, C. Vijila, S. Ramakrishna, Pinhole-free mixed perovskite film for bending durable mixed perovskite solar cells. Sol. Energy Mater. Sol. Cells **175**, 111–117 (2018). https://doi.org/10.1016/j.solmat.2017.10.031

34. B. Chen, M. Yang, S. Priya, K. Zhu, Origin of J–V hysteresis in perovskite solar cells. J. Phys. Chem. Lett. **7**, 905–917 (2016). https://doi.org/10.1021/acs.jpclett.6b00215

35. S. van Reenen, M. Kemerink, H.J. Snaith, Modeling anomalous hysteresis in perovskite solar cells. J. Phys. Chem. Lett. **6**, 3808–3814 (2015). https://doi.org/10.1021/acs.jpclett.5b01645

36. S.A.L. Weber, I.M. Hermes, S.-H. Turren-Cruz, C. Gort, V.W. Bergmann, L. Gilson, A. Hagfeldt, M. Graetzel, W. Tress, R. Berger, How the formation of interfacial charge causes hysteresis in perovskite solar cells. Energy Environ. Sci. **11**, 2404–2413 (2018). https://doi.org/10.1039/C8EE01447G

37. I. Zarazua, G. Han, P.P. Boix, S. Mhaisalkar, F. Fabregat-Santiago, I. Mora-Seró, J. Bisquert, G. Garcia-Belmonte, Surface recombination and collection efficiency in perovskite solar cells from impedance analysis. J. Phys. Chem. Lett. **7**, 5105–5113 (2016). https://doi.org/10.1021/acs.jpclett.6b02193